ELSEVIER

Combustion and Flame 132 (2003) 697–707

Combustion and Flame

# Downward flame spread over a thick PMMA slab in an opposed flow environment: experiment and modeling

K.K. Wu[a], W.F. Fan[a], C.H. Chen[a,*], T.M. Liou[b], I.J. Pan[b]

[a]*Department of Mechanical Engineering, National Chiao-Tung University, HsinChu, Taiwan 30050, R.O.C.*
[b]*Power Mechanical Engineering Department, National Tsing Hua University, HsinChu, Taiwan 30013, R.O.C.*

Received 8 April 2002; received in revised form 18 October 2002; accepted 25 October 2002

**Abstract**

This work investigates experimentally and theoretically the downward spread of a flame over a thick polymethylmethacrylate (PMMA) slab with an opposed flow of air. Simulation results, using an unsteady combustion model with mixed convection, indicate that the ignition delay time increases with a decreasing opposed-flow temperature or increasing velocity. The ignition delay time is nearly constant at a low opposed flow velocity, i.e., $\overline{u_\infty} \leq 30$ cm/s. Experiments were conducted at three different opposed flow temperatures and velocities, namely, $\overline{T_i} = 313$, 333, and 353 K and $\overline{u_\infty} = 40$, 70, and 100 cm/s, respectively. Measurements included the flame-spread rate and temperature distributions, using thermocouples and laser-holographic interferometry. The qualitative trends of the flame-spread rate and thermal boundary layer thickness, as obtained experimentally and from numerical predictions, were identical. For a quantitative comparison, the predicted and experimental flame-spread rates correlated well with each other, except at the lowest velocity ($\overline{u_\infty} = 40$ cm/s). The discrepancies between the measured and predicted thermal boundary layer thicknesses decreased with an increasing flow velocity. The quantitative agreement with a high velocity indicates that the spread of an opposed flame is mainly controlled by the flame front, whereas the discrepancies at low flow rates demonstrate the importance of radiation, the finite length of the fuel, and also three-dimensional effects, which were not considered in the model. The temperature profiles around the flame front measured by interferometric photographs indicate a recirculation flow there, as predicted by the simulation. 

*Keywords:* Flame spread; Opposed flow velocity; Opposed flow temperature

## 1. Introduction

This work studied downward flame-spread over an upright, thick, solid fuel with opposed air flow using an unsteady combustion model and a wind-tunnel experiment. The simulation started at ignition and ended when flame-spread was steady; the combustion experiment simply measured the steadiness of the flame-spread. The variables were the temperature and velocity of the opposed flow.

Chen [1] developed a combustion model to clarify flame-spread over a thermally thin solid fuel in an opposed air flow. The flame-spread rate ($\overline{V}_F$) reduces if the opposed flow velocity is increased, and a blow-off limit is reached when the flow velocity increases to a critical value. Heat conduction in the solid fuel is the dominant process near the blowoff limit, while away from the blowoff limit, flame-spread is dominated by gas phase conduction. Predicted results [2,3] were similar to Chen's [1]. Furthermore, Fernandez-Pello et al. [4] measured the downward flame-spread

* Corresponding author. Tel.: +886-3-5712121; fax: +886-3-5721091.
*E-mail address:* chchen@mail.nctu.edu.tw (C.H. Chen).

0010-2180/03/$ – see front matter 
doi:10.1016/S0010-2180(02)00520-5

**Nomenclature**

| | |
|---|---|
| $\overline{A_s}$ | Pre-exponential factor for fuel pyrolysis, 1/s |
| $\overline{B}$ | Pre-exponential factor for gas phase reaction, $cm^3$/mols |
| $C$ | The specific heat ratio of gas mixture to solid fuel |
| $C_{GD}$ | Gladstone Dale constant |
| $\overline{C_p}$ | Specific heat for gas mixture, J/gK |
| $\overline{C_s}$ | Specific heat for solid fuel, J/gK |
| $Da$ | Damköhler number |
| $\overline{E}$ | Activation energy for gas phase, J/mol |
| $\overline{E_s}$ | Activation energy for solid phase, J/mol |
| $f$ | Stoichiometric oxidizer/fuel mass ratio |
| $g$ | Acceleration due to gravity, $cm/s^2$ |
| $Gr$ | Grashof number |
| $\overline{k_s}$ | Solid phase conductivity, W/cmK |
| $\overline{L}$ | Latent heat, J/g |
| $Le$ | Lewis number |
| $\overline{m''_s}$ | Mass flux, $g/cm^2$ |
| $\overline{P}$ | Pressure, Pa |
| $Pr$ | Prandtl number |
| $\overline{q}$ | Heat of combustion per unit mass of fuel, J/g |
| $\overline{q_{ex}}$ | External heat flux, $W/cm^2$ |
| $Re$ | Reynolds number |
| $S_i$ | Fringe order |
| $S_i - S_{i-1}$ | Fringe shift |
| $t$ | Time, s |
| $\overline{T}$ | Gas phase temperature, K |
| $\overline{T_s}$ | Solid phase temperature, K |
| $\overline{T_r}$ | Reference temperature, K |
| $\overline{T_v}$ | Vaporization temperature, K |
| $\overline{u}$ | Velocity parallel to the fuel surface, cm/s |
| $\overline{v}$ | Velocity normal to the fuel surface, cm/s |
| $\overline{W}$ | Tunnel width, mm |
| $\overline{x}$ | Coordinate parallel to the fuel surface, cm |
| $\overline{y}$ | Coordinate normal to the fuel surface, cm |
| $Y_F$ | Fuel mass fraction |
| $Y_O$ | Oxygen mass fraction |

***Greek symbols***

| | |
|---|---|
| $\overline{\alpha}$ | Thermal diffusivity of gas phase, $cm^2/s$ |
| $\gamma$ | Temperature ratio, $\overline{T^*}/\overline{T_\infty}$ |
| $\overline{\delta}$ | Boundary layer thickness, cm |
| $\overline{\lambda}$ | Wavelength, nm |
| $\overline{\mu}$ | Dynamic viscosity, g/cms |
| $\overline{\rho}$ | Density of gas phase, $g/cm^3$ |
| $\overline{\rho_r}$ | Air density evaluated at $\overline{T_r}$, $g/cm^3$ |
| $\overline{\rho_s}$ | Density of solid phase, $g/cm^3$ |
| $\overline{\tau}$ | Solid fuel thickness, cm |
| $\dot{\omega}_F$ | Non-dimensional gas phase reaction rate |

**Overhead**

| | |
|---|---|
| — | Dimensional quantities |

**Superscript**

| | |
|---|---|
| * | Reference state |

**Subscript**

| | |
|---|---|
| $i$ | Gas-solid interface |
| max | Maximum |
| min | Minimum |
| r | Reference |
| s | Solid phase |
| sf | Burnout |
| $\infty$ | Ambient condition |

rate over vertical PMMA cylinders and found that the flame-spread rate decreases with increasing opposed flow velocity in the larger-flow velocity regime. The effect of the opposed flow is insignificant when the flow velocity is smaller than the induced velocity. Other experimental results [5,6] have indicated that with low flow-velocities of ~10–40 cm/s, the flame-spread rate over a thick PMMA slab remains constant under a specified oxygen concentration, owing to buoyancy, while the spread-rate increases with oxygen concentration. The flame-spread rate first increases with flow velocity, then peaks, and finally decreases with increasing gas velocity under high oxygen concentration, whose mass fraction is greater than 0.432. On the other hand, the flame-spread rate decreases with increasing gas velocity when the oxygen concentration is low. Similar experiments performed with thin paper revealed a constant flame-spread rate for flow velocities of 10–50 cm/s. Above this range, the flame-spread rate decreases with increasing gas flow velocity. The flame-spread rate is found to increase with oxygen concentration when the gas flow-rate is constant.

Di Blasi [7–9] and Lin and Chen [10] investigated how the thickness of the solid fuel influenced the behavior of spreading flames under natural and forced convection. Three main flame-spread regimes were identified. First, where the solid fuels are very thin, the flame-spread rate increases with a thicker solid fuel. Second, if a fuel is thin, the flame-spread rate decreases when the thickness of the solid fuel is increased. Third, the flame-spread rate becomes almost constant once the fuel thickness increases to a certain point. Recently, Lin and Chen [11] developed an unsteady two-dimensional combustion model, describing radiative ignition and the subsequent transition to flame-spread over a vertical, thermally thick, solid fuel under normal gravity. The entire process was divided into two distinct stages. First, in the

heating stage, the maximum temperature increases with time, but the rate of increase slows because of the pyrolysis reaction. In the second stage, a flame develops; there are ignition and transition processes. During ignition, the maximum temperature in the gas phase increases rapidly and significantly, because considerable heat is generated from the chemical reaction of an accumulated flammable mixture. The flame transforms from a premixed flame to a diffusion flame, except for the small region around the flame front. The flame then spreads in two directions, downwards and upwards, to further support itself. Nakamura et al. [12] numerically studied the ignition of a horizontal solid fuel heated by external radiation. Two distinct types of ignition were identified. The first one occurs when the oxygen concentration is relatively high and the position of ignition is at the tip of the plume, with a short ignition delay time. The second one occurs when the oxygen concentration is low and ignition occurs inside of the plume, with a relatively long ignition delay time. The first type of ignition is controlled by one-dimensional heat and mass transport, whereas the second type is controlled by a two-dimensional process caused by buoyancy-induced flow. Fujita et al. [13] experimentally studied the radiative ignition of a paper sheet in a quiescent microgravity environment. They used a $CO_2$ laser as the ignition source at various oxygen concentrations and pressures. The experimental results indicated that the ignition delay time decreases with an increase in oxygen concentration or pressure.

Several experiments [14–17] have investigated the effects of the temperature of the opposed flow on a flame's behavior; it was found that ignition delay time decreases and flame-spread rate increases with the temperature of the opposed flow.

This study utilized an unsteady combustion model to investigate the downward spread of a flame over a PMMA slab in a mixed convection environment. The entire process was studied, from ignition to subsequent flame spread, and the behavior of the flame at each stage was examined in detail. It was followed by experiments that measured the steady opposed-rate of flame-spread and also the temperature distribution for different velocities and temperatures of the opposed flow. Finally, the experimental measurements were compared with predicted results to identify the controlling mechanisms and characteristics of downward spreading flames and to verify the applicability of the combustion model.

## 2. Mathematical model

Fig. 1 illustrates the physical configuration of two-dimensional ignition over a vertically solid fuel

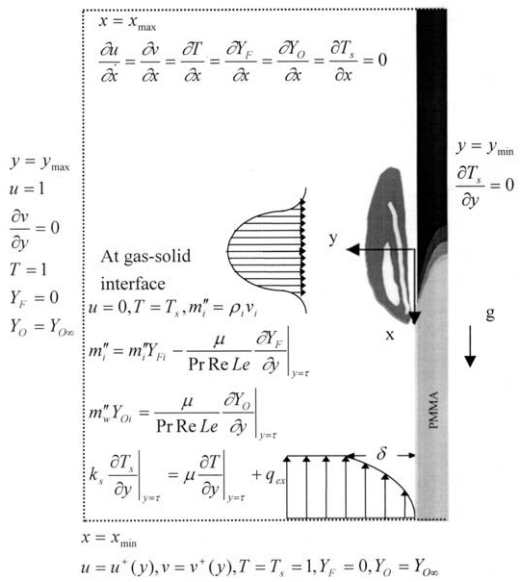


Fig. 1. Schematic of flame-spread over a thick PMMA slab in the mixed-air flows.

in a mixed-convective environment. For $t < 0$, steady flow with a boundary layer builds up over the solid fuel. For $t \geq 0$, an external heat flux with a Gaussian distribution, in which the width is 2 cm and the peak value is 5 $W/cm^2$, is imposed on the solid surface. The unsteady combustion model was basically modified from that developed by Lin and Chen [11] and considers mixed convection. The mathematical model consists of both gas- and solid-phase equations, which are coupled together at the interface. Table 1 summarizes the non-dimensional governing equations for the gaseous and solid phases. The corresponding assumptions and normalization procedures can be found in Fan [18] and are not presented here for brevity. Fig. 1 presents the boundary conditions, which are initially as follows:

For the gas phase:

$$t = 0,\ u \cong u^+(y),\ v \cong v^+(y),\ T = 1,\ Y_F = 0,$$
$$Y_O = Y_{O\infty} \tag{1}$$

where $u^+(y)$ and $v^+(y)$ are adopted from Blasius profiles across the flow [19].

For the solid phase:

$$t = 0,\ \rho_s = T_s = 1 \tag{2}$$

The numerical scheme adopts the SIMPLE algorithm [20]. The unsteady governing equations, as well as the interfacial and boundary conditions, are solved at each time-step until a convergence criterion (residual $< 0.01$) is satisfied, after which they are advanced to the next time step. The smallest grid size

Table 1
Nondimensional governing equations

Gas-phase-governing equation

$$\frac{\partial}{\partial t}(\rho\phi) + \frac{\partial}{\partial x}\left(\rho u\phi - \Gamma\frac{\partial\phi}{\partial x}\right) + \frac{\partial}{\partial y}\left(\rho v\phi - \Gamma\frac{\partial\phi}{\partial y}\right) = S$$

| Equation | $\phi$ | $\Gamma$ | $S$ |
|---|---|---|---|
| Continuity | 1 | — | 0 |
| $x$-momentum | $u$ | $\frac{\mu}{\mathrm{Re}}$ | $-\frac{\partial P}{\partial x} + S_u + \frac{Gr}{\mathrm{Re}^2}(\rho_\infty - \rho)$ |
| $y$-momentum | $v$ | $\frac{\mu}{\mathrm{Re}}$ | $-\frac{\partial P}{\partial y} + S_v$ |
| Energy | $T$ | $\frac{\mu}{\mathrm{Pr\,Re}}$ | $-q\dot{\omega}_F$ |
| Fuel | $Y_F$ | $\frac{\mu}{\mathrm{Pr\,Re}\,Le}$ | $\dot{\omega}_F$ |
| Oxidizer | $Y_O$ | $\frac{\mu}{\mathrm{Pr\,Re}\,Le}$ | $f\dot{\omega}_F$ |

Solid-phase-governing equations

Mass $$\frac{\partial\rho_s}{\partial t} = -(A_s)\left(\frac{\rho_s - \rho_{sf}}{1-\rho_{sf}}\right)\exp\left(-\frac{E_s}{T_s}\right)$$

Energy $$\rho_s\frac{\partial T_s}{\partial t} = \frac{\partial m_s''}{\partial y}\tau[L + (1-C)(T_s - 1)] + \alpha_s\frac{\partial^2 T_s}{\partial x^2} + \alpha_s\frac{\partial^2 T_s}{\partial y^2} - (Cm_s''\tau)\frac{\partial T_s}{\partial y}$$

Where

$$S_u = \frac{1}{3}\frac{\partial}{\partial x}\left(\frac{\mu}{\mathrm{Re}}\frac{\partial u}{\partial x}\right) + \frac{\partial}{\partial y}\left(\frac{\mu}{\mathrm{Re}}\frac{\partial v}{\partial x}\right) - \frac{2}{3}\frac{\partial}{\partial x}\left(\frac{\mu}{\mathrm{Re}}\frac{\partial v}{\partial y}\right)$$

$$S_v = \frac{1}{3}\frac{\partial}{\partial y}\left(\frac{\mu}{\mathrm{Re}}\frac{\partial v}{\partial y}\right) + \frac{\partial}{\partial x}\left(\frac{\mu}{\mathrm{Re}}\frac{\partial u}{\partial y}\right) - \frac{2}{3}\frac{\partial}{\partial y}\left(\frac{\mu}{\mathrm{Re}}\frac{\partial u}{\partial x}\right)$$

$\dot{\omega}_F = -Da\rho^2 Y_F Y_O \exp(-E/T)$.

Equation of state: $\rho \cong \gamma/T$.

The equation for viscosity variation with temperature: $\mu = T/\gamma$.

is 0.1 mm. Grid points are mostly clustered in the external radiative heating region. A grid-size independence test was conducted in advance, and the selection of a non-dimensional time step of $\Delta t = 9$ (equivalent to a real time 0.05 s) and a non-uniform grid distribution of $176 \times 77$ was found to achieve an optimal balance between resolution, computational time, and memory space requirements. The computation was performed on a personal computer.

## 3. Apparatus

Fig. 2 schematically depicts the experimental setup. Air at room temperature was drawn into the test section through a heater, flow straightener, and four screens in the settling chamber and a 16:1 contraction by a 3-hp blower at the downstream end. The heated air then flowed over the PMMA surface, through a flow straightener, a rotameter, and a bellows, and was finally exhausted by the blower. Thermocouple probing and laser holographic interferometry were used to measure local gas temperatures in the test section. T-type thermocouples, made of 0.25-mm-diameter wires, were used for a temperature traverse across the test section, and K-type thermocouples, made of 0.08-mm-diameters wires, were used for measuring the wall temperature. The accuracy of positioning the thermocouple beads was ±0.1 mm. For non-intrusive measurements by laser holographic

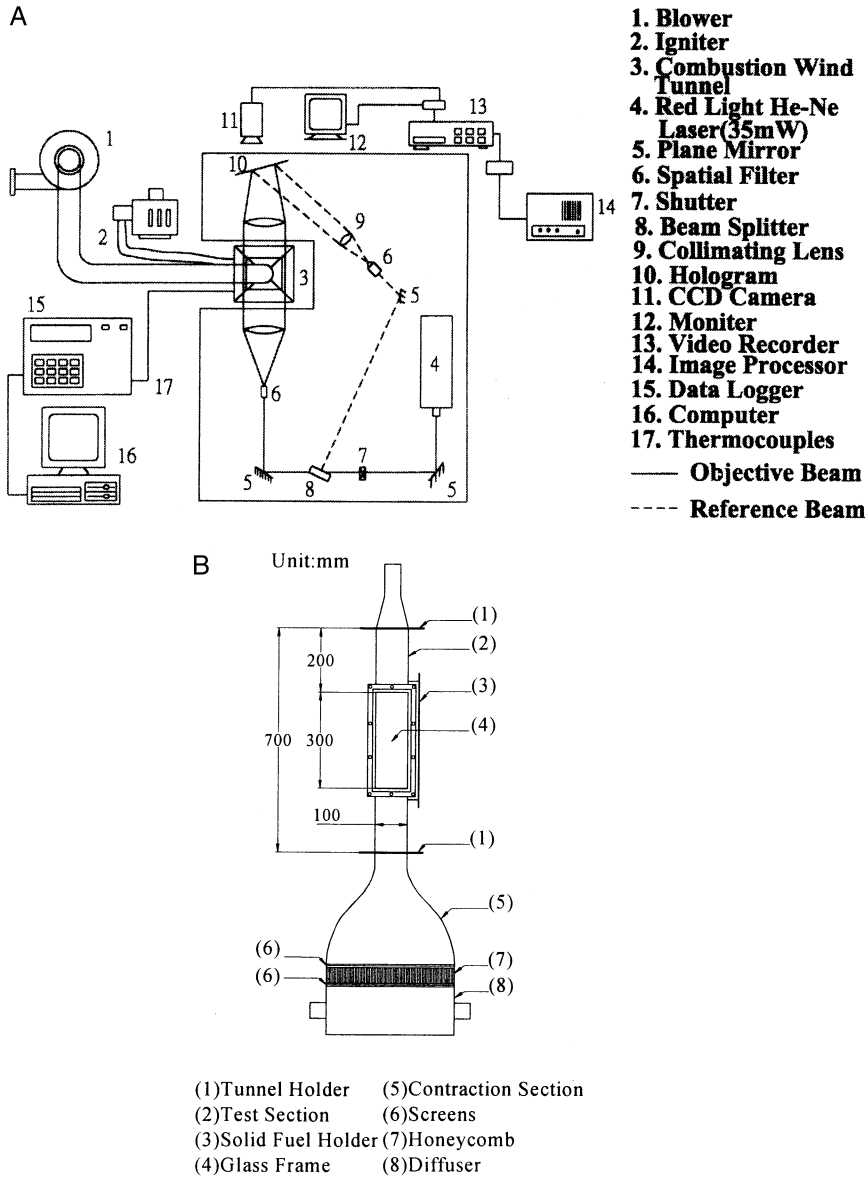


Fig. 2. (a) Schematic drawing of over-all experimental system. (b) Schematic drawing of wind tunnel. The dimensions are in mm.

interferometry, a 35mW He:Ne laser beam (632.8-nm wavelength) was split and expanded into two beams of 150-mm diameter with plane wavefronts after passing through a shutter. The object beam passed through the test section, while the reference beam bypassed it. The two expanded beams then interfered on a hologram plate. The entire test section was mounted on a modified milling machine with four vibration-isolation mounts to allow successive scanning of the expanded object beam.

The holographic film plate holder and liquid gate were used in combination to provide in-place development of the film plate as required for real time holographic interferometry. The photographic emulsion was 10E75, made by Agfa-Gevaert Limited. Through a CCD camera (Chou, model 6400) with a 512 × 512 pixel resolution and 256 grey levels per pixel, the instantaneous interference field was monitored on a multi-sync monitor and recorded on a VHS videocassette recorder for storage and further image processing. To determine the temperature field described by the interferogram after image binarization

and thinning, the equation of interferometry for a two-dimensional incompressible flow is [21,22]:

$$S_i - S_{i-1} = \frac{\overline{T_r \rho_r} C_{GD} \overline{W}}{\overline{\lambda}} \left( \frac{1}{\overline{T}_{S_i}} - \frac{1}{\overline{T}_{S_{i-1}}} \right) \tag{3}$$

By setting $S_i - S_{i-1} = 1$, the temperature differences $\overline{T}_{S_i} - \overline{T}_{S_{i-1}}$ associated with each fringe were determined. Knowledge of at least one temperature and the temperature difference in the region of interest provided the temperature distribution from the fuel's surface to the air.

The test channel was 700 mm long and had a $100 \times 100$ mm$^2$ ($x$–$y$ plane) rectangular cross section. The specimens were mounted on the groove of the test section, and the sides of this groove were covered with asbestos plates to avoid side effects. Ignition was performed by an electrically heated Ni-Cr wire, placed above the specimen for the downward flame propagation experiment. For ignition, the Ni-Cr wire was subjected to a 15V A.C. current for about 20 s, after which the current was cut off. This current was sufficient to cause ignition, and the burning surface was smooth. The specimens were PMMA slabs with the following dimensions: length 30 cm, width 3 cm, and thicknesses 0.82 cm and 1.74 cm. The K-type thermocouples were embedded in the center-line of the PMMA surface to measure surface temperature, and the thermocouples were spaced 5-cm apart. A thermocouple signal was recorded on a multi-channel Yokogawa DA-2500 analyzing recorder, and the flame-spread rate was obtained by dividing 5 cm (the distance between two thermocouples) by the time recorded to have elapsed between the peaks on each of the two temperature traces. The combustion experiments were performed at National Tsing Hua University.

## 4. Results and discussion

The properties of gaseous and solid phases used for computation are $\overline{E_s} = 1.298 \times 10^5$ J/mol, $\overline{A_s} = 2.282 \times 10^9$ s$^{-1}$, $\overline{L} = 941.08$ J/g, $\overline{k_s} = 2.675 \times 10^{-3}$ W/(cm K), $\overline{C_s} = 1.465$ J/(g K), $\overline{\rho_s} = 1.19$ g/cm$^3$, $\overline{T_v} = 668$ K, $\overline{C_p} = 1.183$ J/(g K), $\overline{E} = 8.895 \times 10^4$ J/mol, $\overline{B} = 5.928 \times 10^{12}$ cm$^3$/(g s), $\overline{q} = 2.59 \times 10^4$ J/g, and $f = 1.92$, and were adopted from West et al. [23] and Fernandez-Pello et al. [5]. Meanwhile, the ambient-oxygen concentration was fixed at 0.233. Parametric studies were performed by changing the temperature ($\overline{T_i}$) of the opposed flow and velocity ($\overline{u_\infty}$), which are exactly the same as those used experimentally. Notably, the plate of fuel in the simulation was extended infinitely in both directions in the simulation, whereas it is finite in an experiment.

Fig. 3 displays the ignition delay time as functions of the temperature and velocity of the opposed flow. Note that ignition has been described before [11] and will not be considered here. For studying the effect of temperature on opposed flow, the velocity of opposed flow and the fuel's thickness were fixed at 70 cm/s and 0.82 cm, respectively, and the temperature was varied from 298 to 373 K. The ignition delay-time was found to gradually decay with increasing temperature for opposed flow. This phenomenon occurred because the fuel was preheated from a long way upstream, and thus, less time and/or energy was needed to achieve the surface temperature required for pyrolysis. Therefore, the formation time for a flammable mixture was shortened, and ignition became easier in a hotter opposed-flow. The above trend has been confirmed by the experiments of Pan [24], Chen [25], and Brehob et al. [15].

Regarding the effect of velocity on opposed flow, the temperature was fixed at 313 K while the velocity was varied from 5 to 100 cm/s. The predicted result demonstrated that the ignition delay-time increased with the velocity of opposed flow. However, the ignition delay time remained almost constant when $\overline{u_\infty} \leq 30$ cm/s, a magnitude approximately equal to the induced flow velocity. Restated, if the opposed flow velocity is less than the induced flow velocity, then the influence of opposed flow is insignificant. Since the boundary layer is not very thin in the low opposed flow regime, fuel vapor can accumulate just above the pyrolysis region to form a flammable mixture, which is not carried downstream. Therefore, ignition is not influenced by the magnitude of velocity in that regime. In the highly opposed flow regime, the boundary layer becomes so thin that the accumulation of fuel vapor becomes difficult, extending the formation time for the flammable mixture and so delaying ignition. This has been confirmed by the experiments of Kashiwagi et al. [26] and Tewarson and Ogden [27], which also indicate that the ignition delay-time is independent of the flow-velocity in the low velocity regime.

Figs. 4a and 4b display the flame-spread rate versus temperature of the opposed flow under different flow-velocities for fuel thicknesses of 0.82 cm and 1.74 cm, respectively. Both the predicted results and experimental measurements are provided and compared below. Generally, the flame-spread rate increases with temperature of the opposed flow in Figs. 4a and 4b, and flame-spread can be regarded as a continuous ignition process. If the solid fuel is preheated by a hotter opposed flow, then the heat loss from the flame to the solid is reduced, and the upstream, unburned solid fuel is easier to ignite. Con-

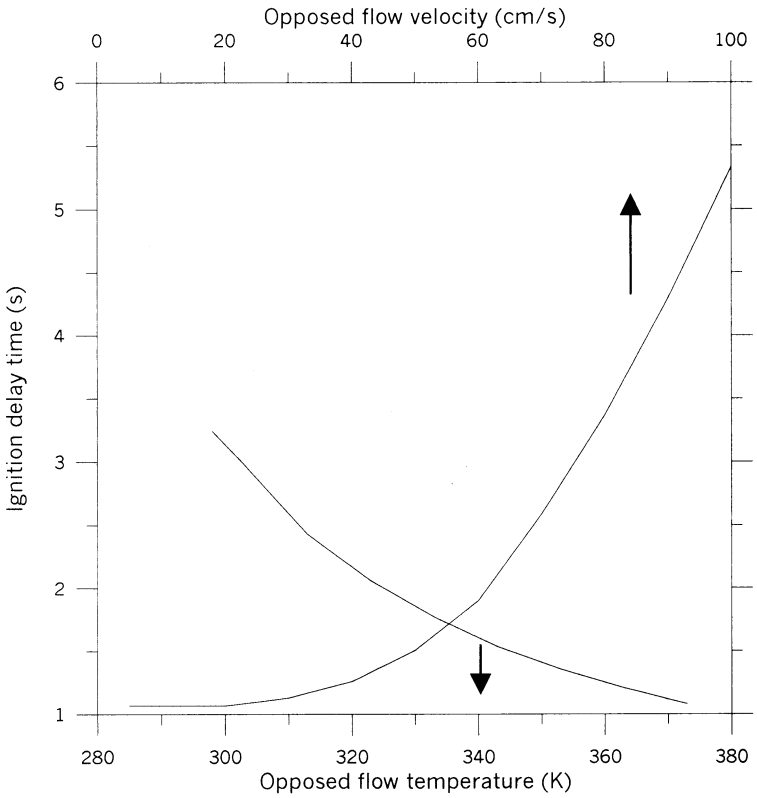


Fig. 3. Ignition delay-time versus opposed-flow temperature ($\bar{\tau} = 0.82$ cm, $\overline{u_\infty} = 70$ cm/s) and opposed-flow-velocity ($\bar{\tau} = 0.82$ cm, $\overline{T_i} = 313$ K).

sequently, the flame-spread rate increases. Regarding these experiments, Niioka et al. [14], Pan [24], Chen [25], Magee and McAlevy III [16], and Perris and Pettett [17] reached the same conclusion, despite using different materials to measure flame-spread rate at different temperatures of opposed flow.

With a fixed opposed flow temperature, the downward flame-spread rate decreased with increasing opposed flow velocity. This occurred because the higher opposed flow velocity increases flame stretch and thus, reduces the flame-spread rate. Furthermore, the steady flame-spread rate decreases with increasing fuel thickness under the same opposed flow velocity and temperature. When the fuel becomes thicker, the heat lost to the solid fuel increases, thus weakening the flame. Meanwhile, solid fuel takes longer to pyrolyze, slowing the flame-spread rate over the thicker fuel.

The predictions and measurements are now compared. The qualitative trend is clearly identical for both the experimental measurements and numerical predictions. The physical interpretations were given above. For a quantitative comparison, the agreement between the predicted and experimental results is generally quite good. The discrepancies are less than 7%, except in the low velocity regime ($\overline{u_\infty} = 40$ cm/s) for fuel thicknesses of 0.82 cm and 1.74 cm. Radiation, which is not considered in the present model, is believed to play a very important role in preheating upstream virgin fuel in the low velocity regime. On the other hand, radiation is relatively less important in the high velocity regime, so the discrepancy between predictions and measurements decreases with a faster opposed flow. The other reason for this discrepancy may be that the upstream boundary layer thickness is fixed in the simulation, but it was varied in the experiment, owing to different inlet velocities. Also, the boundary layer may not be fully established in the experimental test section, especially in the low velocity regime. This can influence the behavior of the flame front, significantly influencing the flame-spread rate. Meanwhile, the downstream tail of the flame over the finite length of the specimen is expected to differ from that in the simulation; particularly when the opposed flow velocity is low, the downstream influence may be sufficient to influence the behavior of the flame front upstream. Besides, the sample is narrow. The three-dimensional

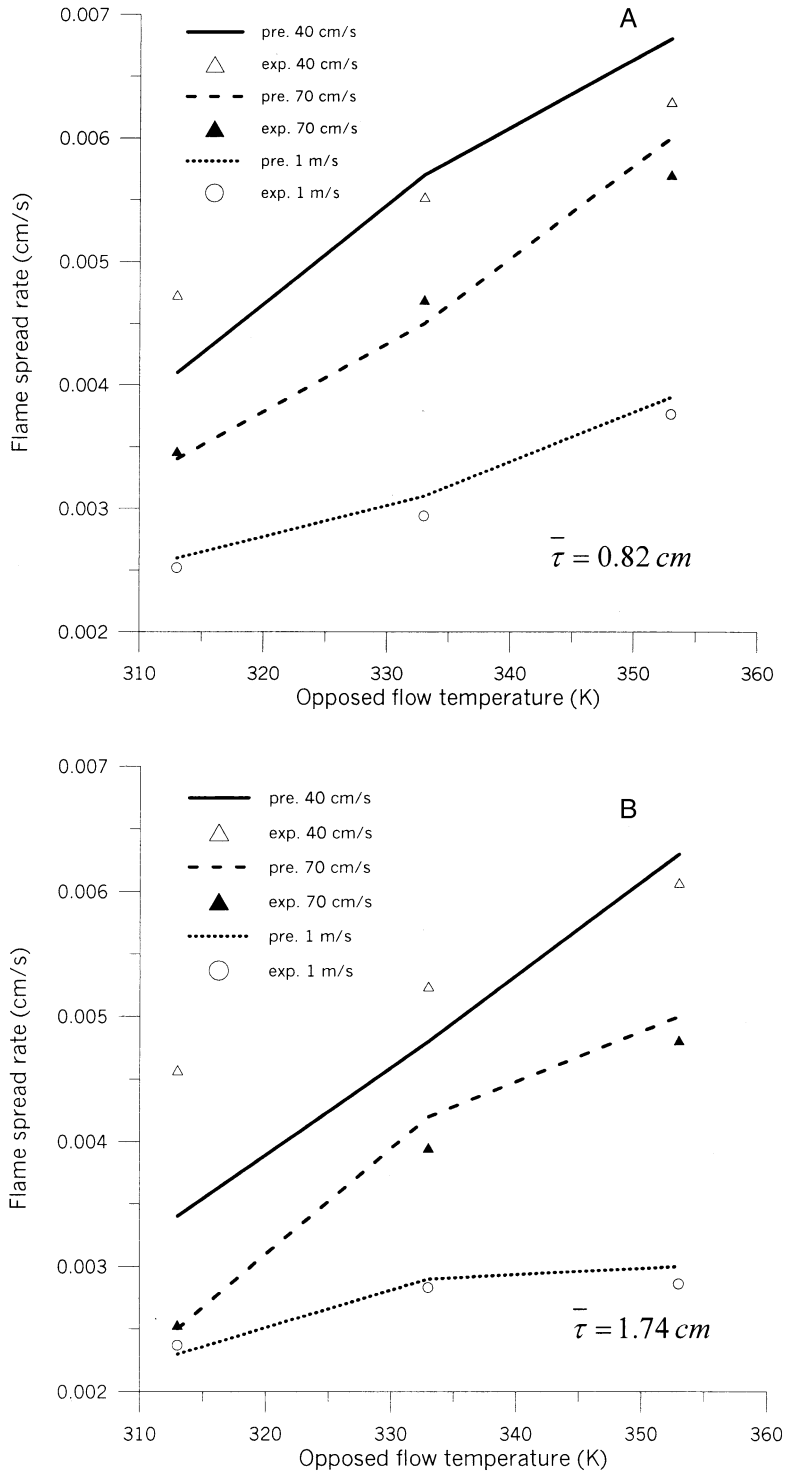


Fig. 4. Flame-spread rate versus opposed-flow temperature under different flow-velocity for (a) $\bar{\tau} = 0.82$ cm and (b) $\bar{\tau} = 1.74$ cm. The experimental points are △ for 40 cm/s, ▲ for 70 cm/s, and ○ for 1 m/s. The lines were computed from the model.

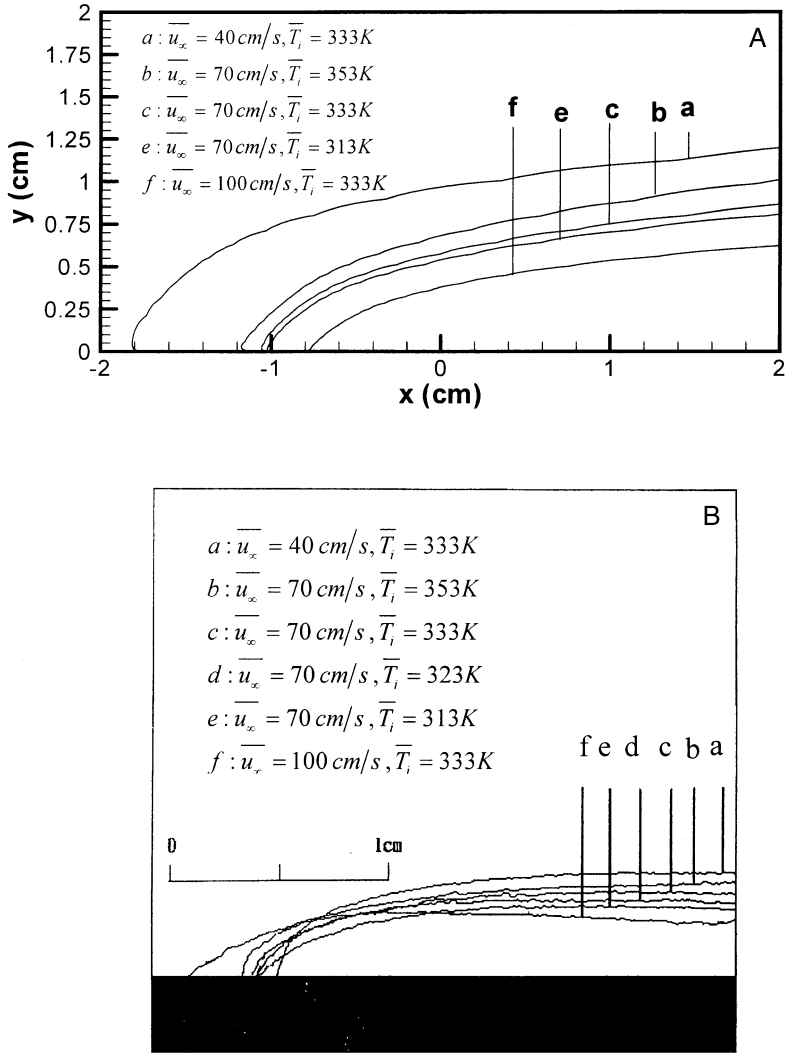


Fig. 5. Thermal-boundary-layer position in $\overline{\tau} = 0.82$ cm for (a) predictions and (b) experiments.

effect from induced flow will become significant when the velocity of the opposed flow is low. The flame pattern is not exactly two-dimensional. However, our model is two-dimensional and cannot capture three-dimensional phenomena. This causes the discrepancies between experimental and predicted results with low velocities for opposed flow. Therefore, the three-dimensional effect can never be neglected in the low velocity region.

Figs. 5a and 5b, respectively, present the computed and measured thermal boundary layer positions for various temperatures and velocities of opposed flow. The thermal boundary layer's position is defined as the displacement from the fuel surface to the position of the temperature contour, $\overline{T}$, when $\overline{T} - \overline{T_i} = 0.1(\overline{T_{\max}} - \overline{T_i})$, where $\overline{T_i}$ denotes the opposed flow temperature and $\overline{T_{\max}}$ denotes the maximum flame temperature. This definition was used for the experiment because of the imaging process. The qualitative trends are clearly identical in Fig. 5 for both experiment and prediction.

As expected, the thermal boundary layer thickens with a hotter opposed flow (cases b, c, and e in Fig. 5). The temperature increases because of the stronger flame resulting from the hotter opposed flow, and heat can be transferred farther in both the streamwise and cross-stream directions. This trend was confirmed by the experiments of Pan [24] and Chen [25].

For the thermal boundary layer positions at different opposed-flow velocities under a fixed flow temperature, 333 K (cases a, c, and f in Fig. 5), the thermal boundary layer becomes thinner when the

flame is subjected to a faster opposed flow, a phenomenon called the flame stretch effect. Both the experimental and predicted results indicate that the flame stretch effect is more effective than the thermal effect.

The boundary-layer thickness at 10 mm from the flame's leading edge in the stream-wise direction is now used for quantitative comparison. Fig. 5 shows that the thermal boundary layer thicknesses are a, 0.4 cm; b, 0.38 cm; c, 0.36 cm; d, 0.33 cm; e, 0.3 cm; and f, 0.27 cm in the experiment, and a, 0.8 cm; b, 0.64 cm; c, 0.56 cm; e, 0.53 cm; and f, 0.44 cm in the simulation. The difference increases when flow velocity is decreased at a fixed temperature. The main reason for this is the fuel configuration, which is finite in the experiment, meaning that the downstream boundary layer is bent toward the inert holding plate and reduces its thickness. In the simulation, the fuel extends infinitely in both directions, and the boundary layer is growing.

Fig. 6 displays interferometric photographs of a downward flame spreading along PMMA slabs ($\overline{\tau}$ = 0.82 cm) for the five cases mentioned in Fig. 5. These photographs were treated with binarization. Clearly, the temperature fields are nearly invariant when $\overline{T_i}$ increased from 313 to 333 K (cases c and d) for $\overline{u_\infty}$ = 70 cm/s. However, when $\overline{T_i}$ rises further to 353 K (case b), the interference fringes move farther away from the fuel surface, and the curvature of the fringes increases. This occurs because the blowing velocity of the fuel vapors from the pyrolyzing surface intensifies at $\overline{T_i}$ = 353 K, pushing the temperature contours farther away from the surface. Notably, the maximum flame temperature increases with the temperature of the opposed flow, as discussed previously.

For the interferometric photographs for $\overline{u_\infty}$ = 40, 70, and 100 cm/s (cases a, c, and e) and $\overline{T_i}$ = 333 K, the thermal boundary layer's thickness clearly reduces, and the temperature contours tend to be parallel to the fuel surface when the opposed flow velocity is increased. The former phenomenon is caused by flame stretch, while the latter, a thermal stratification effect, is caused by the finite size of the test specimen.

Fig. 7 illustrates the predicted and experimental temperature contours of the gas-phase for $\overline{\tau}$ = 0.82 cm, $\overline{T_i}$ = 333 K at a high velocity, and $\overline{u_\infty}$ = 100 cm/s. Notably, the interferometric photograph on the right-hand side is treated by thinning as well as binarization, and it is not scaled. Notably, the low temperature isotherm, like that for $\overline{T}$ = 367 K, is found to be slightly distorted near its apex in both the simulation and the experiment. This is caused by recirculation flow just ahead of the flame front, as predicted by simulation. The flow brings some hotter

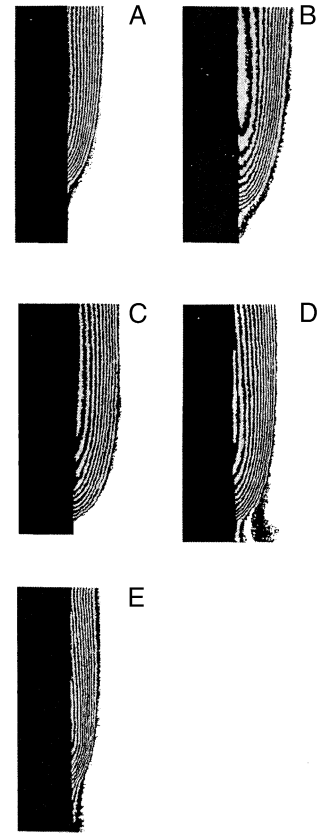


Fig. 6. Interferometric photographs for downward flame-spread along PMMA slabs in $\overline{\tau}$ = 0.82 cm for (a) $\overline{u_\infty}$ = 40 cm/s, $\overline{T_i}$ = 333 K, (b) $\overline{u_\infty}$ = 70 cm/s, $\overline{T_i}$ = 353 K, (c) $\overline{u_\infty}$ = 70 cm/s, $\overline{T_i}$ = 333 K, (d) $\overline{u_\infty}$ = 70 cm/s, $\overline{T_i}$ = 313 K, and (e) $\overline{u_\infty}$ = 100 cm/s, $\overline{T_i}$ = 333 K.

product gases upstream while carrying some cold air downstream. Consequently, the low temperature isotherm is twisted backward and extended forward near its apex. The occurrence of flow recirculation also reinforces forward heat transfer in addition to heat conduction, thus stabilizing the flame by enhancing mixing. The protruding pattern of low temperature isotherms near the flame front also can be identified in all the interferometric photographs in Fig. 6.

## 5. Conclusions

This study investigated downward flame-spread over a thick PMMA slab both experimentally and by unsteady numerical modeling. The parametric study was based on a variation of temperature and velocity of opposed flow. The ignition delay time was found to increase when the temperature of the opposed flow

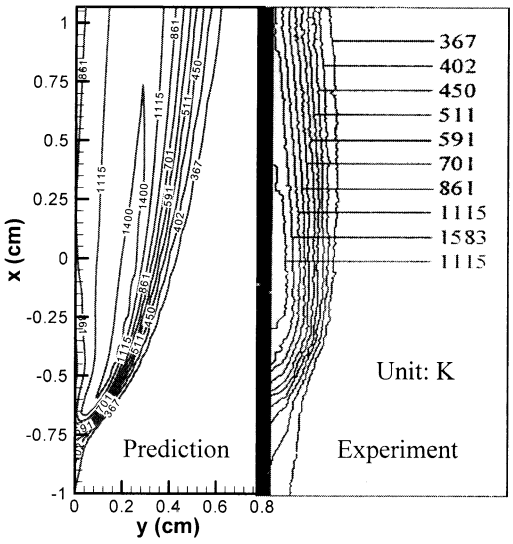


Fig. 7. Temperature contours of the gas phase in $\bar{\tau} = 0.82$ cm, $\overline{T_i} = 333$ K, and $\overline{u_\infty} = 100$ cm/s.

was lowered and also for a faster moving opposed flow. However, the ignition delay time was nearly constant for the low opposed flows ($\overline{u_\infty} \leq 30$ cm/s). Generally, the predicted results and measurements give identical qualitative trends for the flame-spread rate and the thermal boundary layer thickness. The flame-spread rate increased and the thermal boundary layer was thickened by decreasing the velocity or increasing the temperature of opposed flow. The quantitative agreement between simulated and experimental downward flame-spread rates is relatively good, except in the low velocity regime ($\overline{u_\infty} = 40$ cm/s) for fuel thicknesses of 0.82 and 1.74 cm. It was found that the difference between measured and predicted thermal boundary layer thickness decreased with faster opposed-flows. The discrepancy can be attributed to the proposed combustion models overlooking radiation, the size of the fuel, and also three-dimensional effects, especially in low-velocity regimes. Finally, recirculation ahead of the flame front is predicted by the simulation and also confirmed by the isotherms in the flame's leading edge in the interferometric photographs.

## Acknowledgment

The authors would like to thank the National Science Council of the Republic of China for financially supporting this research under contract No. NSC89-2212-E009-058.

## References

[1] C.H. Chen, Combust. Sci. Technol. 69 (1990) 63–83.
[2] S.L. Olson, Combust. Sci. Technol. 76 (1991) 233–249.
[3] K.B. McGrattan, T. Kashiwagi, H.R. Baum, Combust. Flame 106 (1996) 377–391.
[4] A.C. Fernandez-Pello, S.R. Ray, I. Glassman, Combust. Sci. Technol. 19 (1978) 19–30.
[5] A.C. Fernandez-Pello, S.R. Ray, I. Glassman, Eighteenth Symposium (International) on Combustion, The Combustion Institute, Pittsburgh, 1981, pp. 579–589.
[6] S.R. Ray, I. Glassman, Combust. Sci. Technol. 32 (1983) 33–48.
[7] C. Di Blasi, Combust. Flame 97 (1994) 225–239.
[8] C. Di Blasi, Combust. Flame 100 (1995) 332–340.
[9] C. Di Blasi, Fire Safety J. 25 (1995) 287–304.
[10] P.H. Lin, C.H. Chen, Combust. Flame 118 (1999) 744–746.
[11] P.H. Lin, C.H. Chen, Combust. Sci. Technol. 151 (2000) 157–187.
[12] Y. Nakamura, H. Yamashita, T. Takeno, G. Kushida, Combust. Flame 120 (2000) 34–48.
[13] O. Fujita, J. Takahashi, K. Ito, Proceedings of the Combustion Institute, Vol. 28, The Combustion Institute, Pittsburgh, 2000, pp. 2761–2767.
[14] T. Niioka, M. Takahashi, M. Izumikawa, Eighteenth Symposium (International) on Combustion, The Combustion Institute, Pittsburgh, 1981, pp. 741–747.
[15] E.G. Brehob, A.K. Kulkarni, Fire Safety J. 31 (1998) 181–200.
[16] R.S. Magee, R.F. McAlevy III, J. Fire Flamm. 2 (1971) 271–282.
[17] L.E. Perris, K. Pettett, J. Fire Flamm. 5 (1974) 85–96.
[18] W.F. Fan, The study of ignition and flame spread over a thick solid fuel in a forced convective environment, M.S. Thesis, National Chiao Tung University, Hsinchu, Taiwan, R.O.C., 2001.
[19] H. Schlichting, Boundary layer theory, McGraw-Hill, New York, 1950.
[20] S.V. Patankar, Numerical heat transfer and fluid flow, McGraw-Hill, New York, 1980.
[21] W. Hauf, U. Grigull, Advances in heat transfer, in: J.P. Hartnett, T.F. Irvine (Eds.), Advances in heat transfer, Academic, New York, 1970, vol. 6, pp. 133–136.
[22] T.M. Liou, J.J. Hwang, ASME J. Heat Transfer 114 (1992) 56–64.
[23] J. West, L. Tang, R.A. Altenkirch, S. Bhattacharjee, K. Sacksteder, M.A. Delichatsios, Proc. Comb. Inst. 26 (1996) 1335–1343.
[24] I.J. Pan, Experimental analyses of flame spread behavior over solid fuel under opposed flow, M.S. Thesis, National Tsing Hua University, Hsinchu, Taiwan, R.O.C., 1999.
[25] R.J. Chen, Experimental analyses of flame spread behavior over solid fuel under suddenly opposed flow, M.S. Thesis, National Tsing Hua University, Hsinchu, Taiwan, R.O.C., 1999.
[26] T. Kashiwagi, K.B. McGrattan, S.L. Olson, O. Fujita, M. Kikuchi, K. Ito, Proceedings of the Combustion Institute, Vol. 26, The Combustion Institute, Pittsburgh, 1996, pp. 1345–1352.
[27] A. Tewarson, S.D. Ogden, Combust. Flame 89 (1992) 337–259.